

# X-ray nano-spectroscopy study of two solid oxide cells operated for long-term in steam electrolysis

Aline Léon<sup>a,\*</sup>, Sabine Schlabach<sup>b</sup>, Julie Villanova<sup>c</sup>

<sup>a</sup> European Institute for Energy Research, Emmy-Noether-Strasse 11, 76131, Karlsruhe, Germany

<sup>b</sup> Institute for Applied Materials, Institute of Nanotechnology, And Karlsruhe Nano Micro Facility, Karlsruhe Institute of Technology, Hermann-von-Helmholtz-Platz 1, 76344, Eggenstein-Leopoldshafen, Germany

<sup>c</sup> ESRF - the European Synchrotron Radiation Facility, 71 Avenue des Martyrs, 38000, Grenoble, France

## ABSTRACT

### Keywords:

Ni K-Edge nano-x-ray absorption near edge spectroscopy  
Nano-XANES  
Long-term degradation  
Solid oxide electrolysis cell  
Cathode-supported cell  
Electrolyte-supported cell

This study addresses the degradation mechanisms of porous fuel electrode from an electrode (Ni/YSZ) and an electrolyte (Ni/CGO)-supported cell operated for long-term in steam electrolysis mode. Using a nanobeam, spatially resolved X-ray fluorescence and X-ray absorption spectroscopy are combined to acquire high-resolution compositional maps and to probe intra-granular changes with the evolution of the Ni chemical state. This experimental work highlights oxidized states of nickel (i.e. NiO/Ni(OH)<sub>2</sub> species) in the case of Ni/CGO while for Ni/YSZ the chemical state is metallic. In both types of fuel electrodes, the Ni depletion occurs and the depletion length is reduced to around 1 µm in the case of Ni/CGO after 23,000 h in contrast to around 4 µm in the case of Ni/YSZ after 6100 h. In the case of Ni/CGO, the coating of Ni particles by the diffusion of Gd and Ce from the CGO contact layer prevents the Ni migration while in the case of Ni/YSZ the Ni migration is not suppressed. These results are in accordance with in-situ impedance data where the main difference observed between Ni/YSZ and Ni/CGO fuel electrodes is a deactivation of the fuel electrode as non-ohmic losses for Ni/YSZ in contrast to Ni/CGO.

## 1. Introduction

The transition from a carbon-based energy system to a low-carbon and ultimately to a net-zero energy system requires a rapid and widespread change of our current energy system. Among the different alternatives, hydrogen has the potential to store, transport and distribute renewable energy. By that, the early deployment of hydrogen produced from renewable electricity and water electrolysis is foreseen as a transition enabler. Thus, worldwide national strategies have been initiated to increase the hydrogen production capacity, and the European (EU)

electrolyzer manufacturers have pledged to increase their capacity to around 19.3 GW (GW) per year by 2030 [1]. To meet such an objective, there is no simple or single solution but rather multiple technologies and fuels scenarios with a need to synchronize the scaling up of clean energy technologies while scaling back fossil fuels [1].

Three technologies, namely proton exchange membrane electrolysis (PEMEL), alkaline electrolysis (AEL) and solid oxide electrolysis (SOEL), are currently scaled-up to the gigawatt. The GW target requests not only to expand the actual renewable energy and water electrolyzer capacity but also to industrialize the manufacturing process and to reduce the

\* Corresponding author.

E-mail addresses: [aline.leon@eifer.org](mailto:aline.leon@eifer.org) (A. Léon), [sabine.schlabach@kit.edu](mailto:sabine.schlabach@kit.edu) (S. Schlabach), [julie.villanova@esrf.fr](mailto:julie.villanova@esrf.fr) (J. Villanova).

voltage degradation rate of the electrochemical cell under high current density over long-term operation (>10,000 h).

Herein, we consider the high-temperature steam solid oxide electrolysis technology based on oxide ion conduction with ceramic-based materials; this technology is of interest due to its potential to use waste heat from industrial processes, to use the same solid oxide cell to produce hydrogen (electrolysis operation) or electricity (fuel cell operation) and to reduce the CO<sub>2</sub> molecules by the co-electrolysis process. In addition, less critical material is involved in the cell manufacturing in terms of availability and pricing. The solid oxide technology has been first developed for fuel cell operation, and research & developments are ongoing to use the identical cells in electrolysis mode. The reversibility of the cells has been proven by operating in fuel cell and electrolysis mode, which implies similar ohmic and activation overpotentials for both operation modes. Today, the most common electrolysis cell architectures are either planar electrode-(cathode)-supported cell (CSC) or electrolyte-supported cell (ESC). The current state of the art in terms of cell manufacturing, operation parameters, performance, durability and degradation can be found in recent monographs and manuscripts [2–6]. To date, the target of the EU Commission to make the high-temperature technology economically viable in electrolysis mode is to achieve a degradation rate of 9 mV/kh at a current density of 1.0 A/cm<sup>2</sup> and 6.5 mV/kh at a current density of 1.5 A/cm<sup>2</sup> in 2027 and 2030, respectively. Towards these targets, the electrodes, the barrier and contact layers as well as the electrolyte are continuously optimized to reduce the degradation rate by improving the initial powder composition, the layers densification, the contact of the different layers, and so on.

The assessment of the degradation source is fairly complex, due to the multilayer system, the combination of different degradation processes (chemical and/or electrochemical degradation, mechanical failure, microstructure evolution, and so on) and the steam environment in electrolysis mode. The most common tools used for tracing degradation are in operando electrochemical techniques (UI curves for cell performance, in-situ impedance spectroscopy), ex-situ analysis with post-mortem characterization using classical and advanced techniques (e.g. Scanning electron microscopy, X-ray diffraction, X-ray imaging, X-ray spectroscopy) and modelling (microstructure of cell or single repeating unit physically-based models, grey-box models and so on) [7–18]. In addition, analytical techniques such as ambient pressure X-ray photoelectron spectroscopy (APXPS) or near edge X-ray absorption fine structure (NEXAFS) recorded in total electron yield (TEY) with a depth resolution of 50 nm have been also applied in-situ or in operando to correlate the degradation path with the electrochemical reaction [19]. Using models and porous electrodes as well complementary characterization tools listed above and theoretical calculation, several insights along the electrochemical reaction and the degradation processes have been gained in the last years that allowed significant improvements in terms of electrode stability, performance and durability of the electrochemical cell and stack. To achieve the targets of low degradation at high current density, it is necessary to further advance our knowledge in the degradation processes and acquire complementary quantitative data from different classical and advanced characterization techniques. Thus, a multimodal characterization approach down to the nanoscale with high spatial resolution and large view combined with the history of the test object (UI curve,  $U = f(t)$ , in-situ impedance spectroscopy, incidents) is becoming more and more necessary. In this frame, in our previous study we acquired 2D nano X-ray fluorescence (nano-XRF) maps on thin lamellas of the complete porous CSCs and ESCs operated for long-term under practical application conditions in electrolysis [20]. Such 2D maps allowed viewing not only the spatial distribution of all the chemical elements that composed the cell but also their diffusion as well as their co-localization at the interfaces of the different functional layers during the sintering process or during the electrochemical reaction. It was further possible to evaluate the thickness of each layer and to assess their evolution after the long-term operation. By that, the functional layers were highlighted and the secondary layers identified in terms

mainly of Gd, Ce and Sr accumulation. It has been shown that, already before the operation the cells have the following complex structure with additional interlayers.

- For a CSCs: Ni/8 YSZ//8YSZ//Sr//Gd//CGO//LSCF
- For an ESCs: Ni(CGO)//CGO//Ce//Gd//6Sc1CeSZ//Gd//Sr//Ce//Sr//CGO//LSCF

An increase of the Gd-based layer thickness at the interface of the electrolyte was observed at the end of the long-term operation, while the change in the Sr-based layer thickness was not significant. In addition, nanoparticles of Co and Fe were present in the diffusion barrier and electrolyte of the ESC. For the fuel electrode, Ni depletion was observed for the CSC while an agglomeration occurred in the ESC [20].

As a further step of our precedent study, the aim herein is to gain additional knowledge on the processes involved within the Ni/(8Y<sub>2</sub>O<sub>3</sub>)ZrO<sub>2</sub> (labeled Ni-8YSZ) and Ni/Ce<sub>0.8</sub>Gd<sub>0.2</sub>O<sub>1.9</sub> (labeled Ni-CGO) porous fuel electrode operated for long-term in electrolysis mode. Indeed, in the abundant literature about the fate of nickel, three main degradation processes are reported: (i) the nickel depletion at the triple phase boundary (TPB), (ii) the morphology changes of the nickel particles and (iii) the presence of impurities in and around the Ni particles [2,7,10,12,13,21,22]. For each process, different mechanisms or reaction pathways are proposed: as an example, the Ni depletion is explained by mass transfer phenomena with surface diffusion of Ni atoms or Ni(OH)<sub>x</sub> species as well as transport in the gas phase of Ni(OH)<sub>2</sub> species or solid-state diffusion of vacancies [2,4]. Particle surface behavior could be linked to a charge transfer based on an interstitial process and an oxygen or hydrogen ‘spillover’ mechanism that corresponds to an oxygen adatom on Ni to form an oxide ion attached to the surface of YSZ for a CSC [13]. In the proposed mechanisms, the chemical state of nickel should differ from the metallic (Ni<sup>0</sup>) to the oxidized state (Ni<sup>2+</sup>). Few studies [11,23] using model electrodes highlighted the change in the oxidation state of surface Ni under different operating conditions. However, to the best of our knowledge, the chemical state of nickel has not been investigated so far with porous fuel electrodes operated under practical conditions for long-term (>5000 h) in electrolysis mode at high current density. In this study, spatially resolved X-ray fluorescence (nano-XRF) and X-ray absorption near edge spectroscopy (nano-XANES) are combined to probe the evolution of the chemical state of Ni within a large porous fuel electrode surface (70 μm × 60 μm). Especially, nano-XANES at the Ni K-edge (8333 eV) with a beam size of 50 × 50 nm<sup>2</sup> have been applied for the first time to analyze the chemical state of Ni within the core and the shell of nickel particles at different position of the complete hydrogen electrode of a CSC and an ESC operated for 6100 h and 23,000 h, respectively.

## 2. Materials and methods

### 2.1. Samples

The circular CSC were elaborated at Forschungszentrum Jülich. The cells consisted of a Ni/(8Y<sub>2</sub>O<sub>3</sub>)ZrO<sub>2</sub> (labeled Ni/8YSZ) cermet as hydrogen electrode, an 8(Y<sub>2</sub>O<sub>3</sub>)ZrO<sub>2</sub> (labeled 8YSZ) electrolyte layer, a barrier composed of Ce<sub>0.8</sub>Gd<sub>0.2</sub>O<sub>1.9</sub> (labeled CGO) and a La<sub>0.58</sub>Sr<sub>0.4</sub>Co<sub>0.2</sub>Fe<sub>0.8</sub>O<sub>3</sub> (labeled LSCF) oxygen electrode. All the layers described above were deposited by screen-printing on a Ni/8YSZ substrate (1.5 mm thick) [12,24]. The cell architecture can be summarized as follows: Ni/8YSZ (1.5 mm)//Ni/8YSZ (8 μm)//8YSZ (10 μm)//CGO (5 μm)//LSCF (30 μm).

The commercial circular ESCs were produced by the company Keratol (Germany). Using the same labels as for CSCs, the ESC architecture can be written as follows: Ni/CGO (30 μm)//CGO (7 μm)//6Sc1CeSZ (130 μm)//CGO (7 μm)//LSCF (30 μm) where 6Sc1CeSZ corresponds to (6Sc<sub>2</sub>O<sub>3</sub>·1CeO<sub>2</sub>)ZrO<sub>2</sub>.

The CSC and ESC were operated by the European Institute for Energy

Research (EIFER) for 6100 h and 23000 h, respectively [12,24,25]. For comparison, the corresponding non-operated cells were analyzed as a reference. These two architectures are compared in this study in order to highlight the difference in the processes of the Ni-YSZ and Ni-CGO fuel electrode. It is pointed out that these cells are specific in terms of performance and operation time giving access to unique microstructural data. As can be seen in Fig. 1, once dismantled from the cell housing after long-term operation, the two cells used in this study were fully intact with neither pollution, delamination nor fissures at the fuel electrode. The visual aspect of the hydrogen electrode surface is comparable to a non-degraded electrode.

During the course of the operation, incidents can occur that can accelerate the degradation, such as steam starvation and thermal cycles; these incidents can either have a reversible or irreversible impact on the cell performance. The knowledge of the type of incidents during the cell operation is thus of importance to avoid any misleading correlation between the electrochemical performance and the corresponding microstructure. For the 6100 h operated CSC, one kind of incident has been reported as a dry pulse of a duration of 2 min that occurred after 1315 h, 1534 h, 3263 h and 5000 h over the testing period. For the ESC operated for 23000 h steam starvation occurred for a few seconds after 4530 h. Considering the total operation time, it is not too likely that these incidents have a significant impact to be detectable within the post-test characterization of these cells.

Thanks to impedance spectroscopy, time dependence evolution of the resistance related to the electrodes, electrolyte contribution as well as gas diffusion can be distinguished with four ohmic parameters defined as the resistance ( $R_{\Omega}$ , which equals the real part of impedance at high frequency), the area specific resistance (ASR which equals the real part at low frequency where the impedance is ohmic), the gas conversion/diffusion resistance of the electrodes ( $R_{conv/diff}$  occurring at low-frequency relaxation) and the resistance from the charge transfer reaction ( $R_{TF}$ , which is present at intermediate frequency). The measurements recorded in-situ (i.e. without current interruption before the measurement) at the steady-state direct current density indicate that the main difference between the CSC and ESC is the fuel electrode deactivation after the long-term operation of the CSC in contrast to ESC. Table 1 summarizes the different operating conditions, the U-j curves and the measured resistance of the CSC and ESC after the long-term operation of 6100 h and 23000 h, respectively. In both cases, the U-j curves show constant open circuit voltage (OCV) indicating rather constant conditions for gases, no fissures and no development of an electronic conducting path. As can be seen, the degradation due to ohmic losses is present for the CSC and ESC and for the CSC a non-ohmic term is present. The degradation due to non-ohmic losses is dominant for

CSC and it is mainly related to the deactivation of the fuel electrode. Also, the conversion/diffusion resistance does not evolve with time in both types of cells indicating a stable feed gas supply and porosity. It is pointed out that all degradation rates are close to the typical values expected in solid oxide fuel cell (SOFC) mode showing the reversibility between SOFC and solid oxide electrolysis cell (SOEC). To complement the in-situ impedance spectroscopy data and the classical imaging and spectroscopy techniques (i.e., scanning electron microscopy (SEM), Energy dispersive X-ray (EDX), and Transmission electron microscopy (TEM), X-ray photoelectron spectroscopy (XPS)) spatially resolved post-test analysis using nano-XRF and nano-XANES at the Ni K-edge was carried out on the Ni-YSZ and Ni-CGO fuel electrodes. Being complementary, these techniques provide information on different length scale of the sample. Indeed, nano-XRF provide high-resolution compositional analysis in combination with high lateral resolution compared to EDX with access to volume of the sample as well as more sensitivity with a detection limit in the range of a few 10 ppm. Further, the analysis of large areas with a continuous scan provides the statistical information in contrast to TEM. Finally, nano-XANES gives access to the volume of the sample while XPS probes only its surface.

## 2.2. Sample preparation

The two cells made of porous electrodes and tested under real application conditions were prepared by *in situ* lift-out in a focused-ion beam (FIB) system (FEI Strata 400 S) to obtain thin transverse cuts (of 1.5–2  $\mu\text{m}$ ) of the solid oxide cells with all functional layers. The cutting was performed using 30 kV  $\text{Ga}^+$  (gallium) ions. Cross-contamination and redeposited contaminations were further reduced using a cleaning-cross-section milling pattern. Fig. 2 displays the different steps to achieve the thin transverse cut of the CSC operated for 6100 h starting from the region of interest (Fig. 2a) down to the desired thickness (Fig. 2b), the lift-out (Fig. 2c) and the transfer to a molybdenum (Mo) FIB-lift-out grid (Fig. 2d and e). The position of the sample within the grid is highlighted in red in Fig. 2e. Thereafter, the Mo grid was mounted on the sample support of the synchrotron beamline. It should be pointed out that care has been taken to have uniform thin samples. However, due to porosity and related curtaining effects from FIB preparation a fully smooth surface was not easily achieved.

## 2.3. Nano-XRF and Nano-XANES at the ID16B beamline

Nano-XRF and nano-XANES with a large field of view and a high spatial resolution were performed at the ID16B beamline of the European Synchrotron Radiation Facility (ESRF) in Grenoble, France [26].

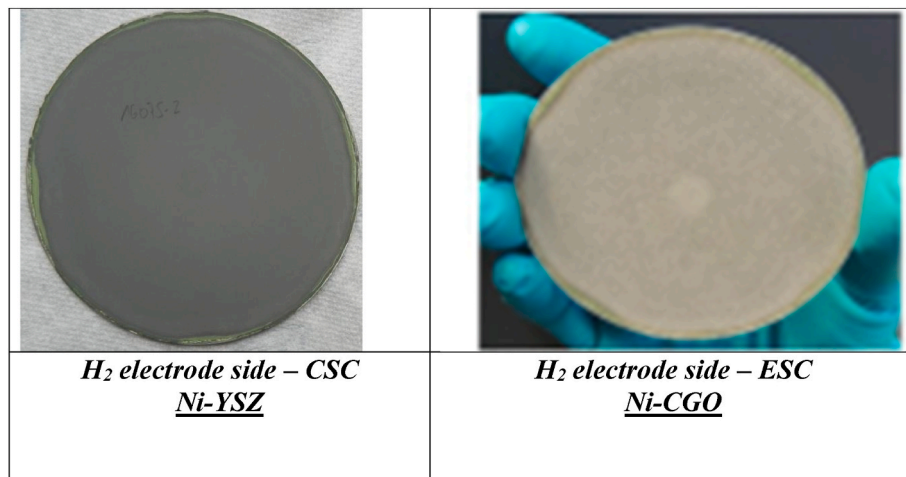
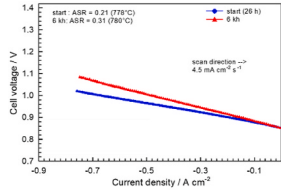
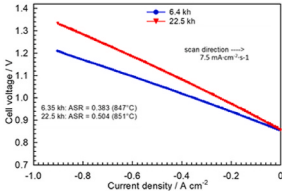
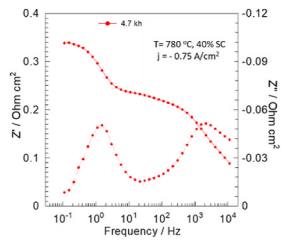
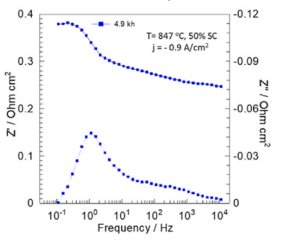


Fig. 1. Pictures of the two cells (diameter of 8 cm) dismantled from the cell housing after 6100 h and 23000 h of operation in electrolysis mode.

**Table 1**

Summary of the operating parameters including U-j curve and in-situ EIS data taken at around 5000 h of operation

Operating parameters	CSC (8YSZ) Fuel electrode: Ni/YSZ	ESC (6Sc1CeSZ) Fuel electrode: Ni/CGO
Temperature (°C)	778–780	847–851
j (A/cm <sup>2</sup> )	0.75	0.9
AH (%)	80	75
SC (%)	40	50
OT (at j above in h)	6100	20,114
Total operation (h)	6150	23,000
U-j curve		
In situ EIS data acquired at about 5000 h of operation		

j current density; AH absolute humidity; SC steam conversion; OT operating time; EIS electrochemical impedance spectroscopy.

An X-ray nanobeam with high flux ( $10^{12}$  photons per second) and a spot size of  $50 \times 50 \text{ nm}^2$  was used with an energy of 17.5 keV to acquire the 2D nano-XRF maps. Fig. 2f displays the lamella of the complete CSC operated for 6100 h and the region of interest (ROI) in red that has been defined as well the corresponding distribution of Ni element in the form of a 2D map. The ROI has been scanned on the transverse cut with a 30 nm step size and a 100 ms acquisition time per point. Analysis of the fluorescence spectra using the PyMca software allows presenting the distribution of each element composing the cell. Thereafter, nano-XANES in targeted points within the 2D maps has been performed at the Ni K-edge ( $E_0 = 8333 \text{ eV}$ ) to probe the chemical state of nickel in the core of the particles as well as at the outer shell along the full fuel electrode. The nano-XANES were acquired by varying the energy from 8280 to 8380 eV with 1 eV and 200 ms per step. Within the thin transverse cut, variations of nickel concentration (strong inside the core of a nickel particle and weak at the interface between the Ni particle, the pores and the ionic conductor) and variations of thicknesses have to be taken into account as they have an impact on the XANES signal with changes in the intensity of the white line (over absorption effect), intensity ratio between the different peaks and signal damping – not only in fluorescence mode but also in transmission mode [27]. Thus, transmitted and fluorescence signals have been recorded for each sample and compared to discriminate the effect of thickness and the self-absorption attenuation on the X-ray absorption signal from the solid oxide samples. The incoming beam signal is recorded thanks to a silicon photodiode detecting the backscattering and fluorescence signals produced by the beam crossing a Titanium foil. The transmitted signal was directly detected with a silicon photodiode placed behind the sample and the fluorescence signal with silicon drift detectors (SDD) placed at  $15^\circ$  from the surface of the sample. The background removal and the normalization of the spectra were performed using standard procedures with the Athena software [28]. The edge position within the spectra was determined with the maximum of the first derivative. The relative concentration of metallic nickel and oxidized states within the samples were analyzed using Athena's linear combination fitting algorithm.

### 3. Results and discussions

#### 3.1. Nano-XANES at the Ni K-edge

For all the samples, both transmitted and fluorescence signals have been acquired and within the manuscript, it has been selected to present the fluorescence spectra because of the quality of the spectra obtained in this mode for points taken at the border of Ni particles due to the sensitivity of the fluorescence mode compared to the transmission one. Further, the effect of the sample thickness could be minimized in this acquisition mode.

##### 3.1.1. Reference spectra of ni, NiO and Ni(OH)<sub>2</sub>

Fig. 3a displays the spectra of metallic nickel (Ni, 6  $\mu\text{m}$  foil), nickel oxide (NiO, powder) and nickel hydroxide (Ni(OH)<sub>2</sub>, powder) samples that have been acquired at the Ni K-edge in fluorescence mode using a nanobeam of  $50 \text{ nm} \times 50 \text{ nm}$ . Silicon nitride, Si<sub>3</sub>N<sub>4</sub> substrate was used to spread the powder samples. Fig. 3b shows the respective first derivatives.

The spectra obtained in fluorescence mode using a nanobeam (Fig. 3a) are comparable to the ones from the literature that are generally obtained using non-spatially resolved XANES [29–31]. Indeed, the metallic nickel is characterized by an edge shoulder at 8333 eV and a double peak at 8350 eV and 8358 eV above the edge (related to the face cubic centered fcc-Ni structure) [32]. The oxides are characterized by a weak peak at 8333 eV (the intensity of which reflects the coordination chemistry of the absorber) and an edge onset shifted by 12 and 14 eV for NiO and Ni(OH)<sub>2</sub> compared to Ni, respectively. The spectra from NiO and Ni(OH)<sub>2</sub> are characterized by an intense white line at 8350 eV with a difference in the shape of the white line as well as the position of the second peak at 8366 eV and 8364 eV for NiO and Ni(OH)<sub>2</sub>, respectively. The three compounds have a common peak at 8350 eV which is used as a reference point for comparing the spectra. Then, each compound has specific characteristics relative to this peak that allow differentiating the oxidation state and separating the phases present in the sample. These results on reference samples validate the reference spectra using nano-XANES.



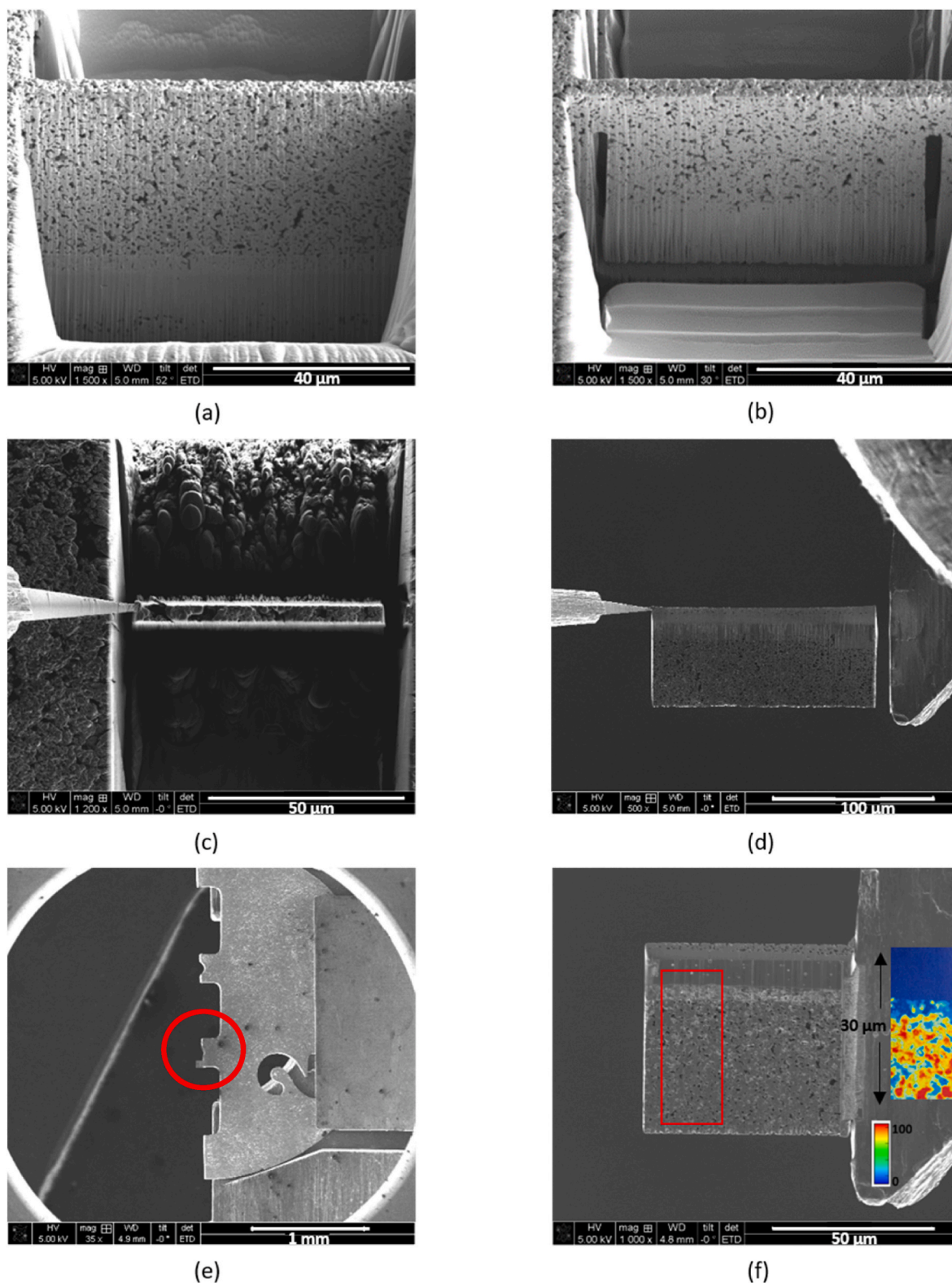
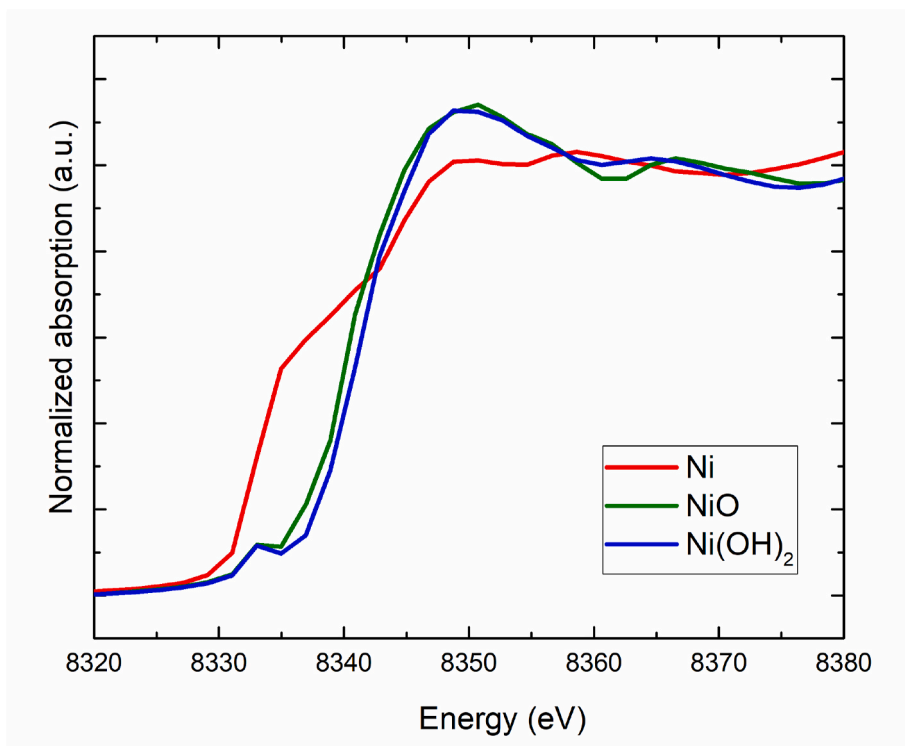


**Fig. 2.** Different steps of the thin transverse cut preparation for sample operated for 6100 h from defining area of interest (a) to FIB milling using Ga ions up to the desired thickness (b), lift-out procedure (c) and transfer to the molybdenum FIB grid (d, e). SEM image of the thin section of sample operated for 6100 h mounted on a Mo FIB grid is included with the region of interest and the corresponding Ni nano-XRF map (f).

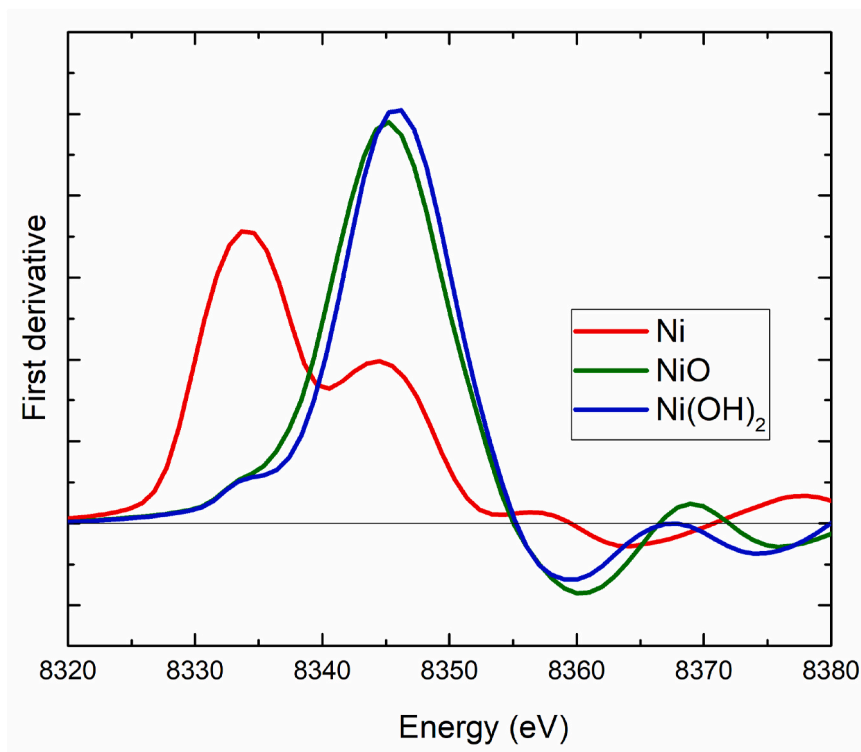
### 3.1.2. Ni K edge Nano-XANES spectra of the non-operated cell

Fig. 4(I) and Fig. 5(I) display the Ni K-edge spectra acquired at different positions of the fuel electrode within non-operated cells CSC and ESC, respectively. As can be seen, in both cases the spectra taken at different positions of the fuel electrode display features that are

characteristic of NiO with a weak peak at 8333 eV and the white line at 8350 eV. The first derivative indicates that the edge is at 8345.63 eV, which corresponds to the shift of 12 eV compared to metallic nickel and the chemical state of  $\text{Ni}^{2+}$ . The topography indicates the presence of larger NiO particles in the case of the ESC compared to the CSC. Further,



a



b

**Fig. 3.** Ni K-edge Nano-XANES fluorescence spectra of metallic Nickel (Ni), Nickel oxide powder (NiO) and Nickel hydroxide powder Ni(OH)<sub>2</sub> (a) and corresponding first derivatives (b).

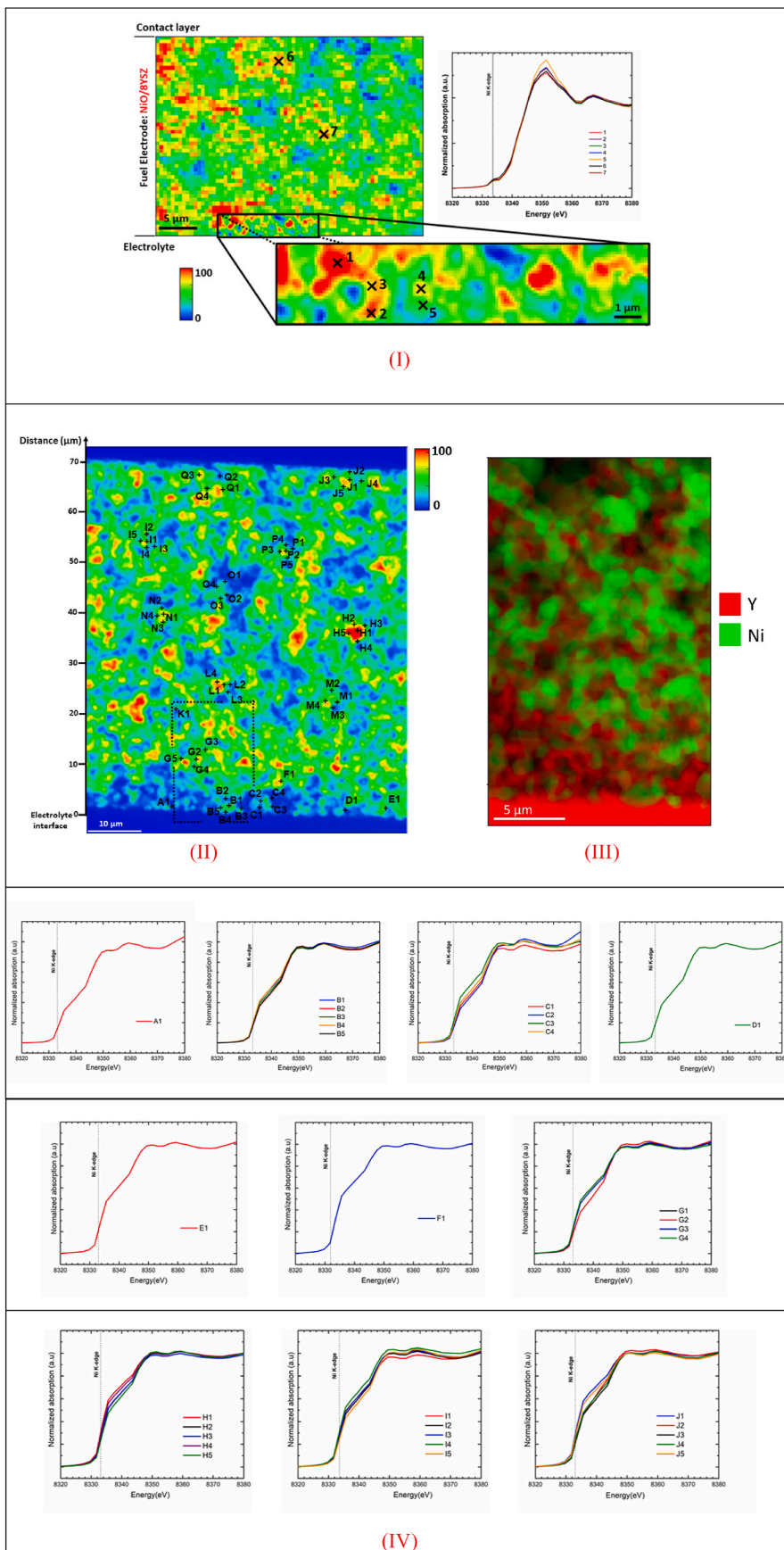


**Fig. 4.** Ni K-edge nano-XANES spectra of the reference CSC and the 6100 h operated cell, without incidence, at the different positions within the electrode with (I) the Ni K-edge nano-XRF map and the XANES spectra of the reference cell (II) the Ni K-edge nano-XRF map of the 6100 h operated cell and the corresponding points where the XANES spectra were acquired with the labels from A to Q from the electrolyte/electrode interface to the top of the substrate (III) the super-imposed nano-XRF maps displaying Y and Ni concentration within the ROI defined in II and (IV) the selected Ni-K-edge nano-XANES spectra from A to J (the spectra from K to Q are shown in Fig. S1).

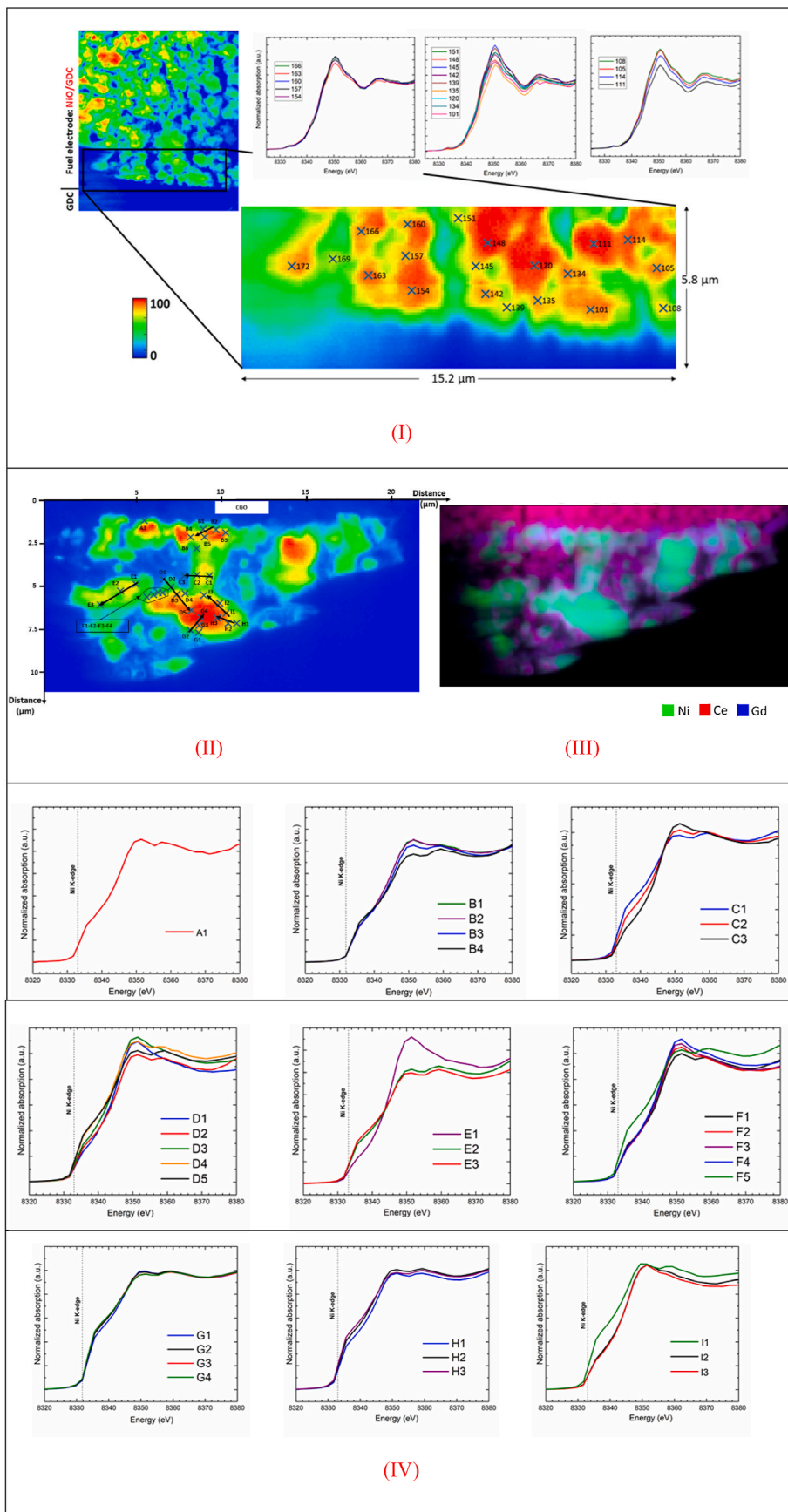


**Fig. 5.** Ni K-edge nano-XANES spectra of the reference ESC and the 23000 h operated cell, at the different positions within the electrode with (I) the Ni K-edge nano-XRF map and the XANES spectra of the reference cell (II) the Ni K-edge nano-XRF map of the 23000 h operated cell and the corresponding points where the XANES spectra were acquired with the labels from A to I (III) the super-imposed nano-XRF maps displaying Gd, Ce and Ni concentration and (IV) the Ni-K-edge nano-XANES spectra.



neither pores nor gaps can be observed between the Ni phase and the YSZ phase while pores are present in the NiO/CGO layer.

### 3.1.3. Ni K edge Nano-XANES spectra of the 6100 h operated CSC

Fig. 4(II) displays the large 2D nano-XRF map ( $70\ \mu\text{m} \times 60\ \mu\text{m}$ ) of the Ni distribution in the active layer and part of the electrode substrate. After the 6100 h operation, the Ni distribution remains homogeneous along the electrode substrate. As expected, the active layer has smaller Ni particles and the cross-section of the grains are in the size from 0.5 to 2  $\mu\text{m}$  while the substrate grain size is coarser from 2.5 to 5  $\mu\text{m}$ . At the interface with the electrolyte, the Ni distribution in the active layer is inhomogeneous with large areas where Ni is lacking. A magnification in this region is shown in Fig. 4(III) to visualize the position of Ni, Y and the pores. As can be seen, the presence of Ni at the electrolyte/electrode interface is at a lower concentration compared to the top of the electrode and the depletion of Ni is present within 4  $\mu\text{m}$  from this interface. The distribution of Y is homogenous with a dense structure at this interface.

58 Ni K-edge XANES spectra were acquired from the electrolyte/electrode interface up to 70  $\mu\text{m}$  of the substrate at different positions in the electrode support and the active layer as shown in Fig. 4(II) with the corresponding labels. Fig. 4(IV) displays 32 selected spectra and the remaining ones are presented in the supplementary information (Fig. S1). The scans are grouped within the same region and labeled from A to Q starting from the electrolyte/electrode interface to the top of the substrate. The analysis of the Ni K-edge spectra in terms of the edge position (taken as the maximum of the first derivative) and peak position compared to the reference one suggests that the chemical state of Ni is metallic within the studied area along the fuel electrode. The variation observed for example in H, I and J group spectra at the rising edge or the white line intensity is mostly related to Ni concentration within the integrated analysis volume.

### 3.1.4. Ni K edge nano-XANES spectra of the 23,000 h operated ESC

Fig. 5(II) displays the 2D nano-XRF map ( $22\ \mu\text{m} \times 11\ \mu\text{m}$ ) of the Ni distribution in the fuel electrode of the 23000 h operated ESC. As can be seen, the distribution of Ni is homogeneous at the interface of the electrode/CGO contact layer and the cross-section of Ni grain size vary from 0.3 to 6  $\mu\text{m}$  within the volume analyzed. Thus, the microstructure of the Ni network is coarser compared to the microstructure of the NiO network from the reference cell. The 2D map with the combined view of the elemental distribution of Ni, Gd and Ce (Fig. 5(III)) clearly indicates the position of the Ni particles, the CGO mixed ionic electronic conductor and the pores. In contrast to Ni particles, the CGO network is made of smaller particles with a homogeneous distribution around the Ni particles. Compared to the reference cell, the CGO concentration is significantly increased and the distribution is denser along the Ni particles. 31 Ni K-edge XANES spectra (Fig. 5(IV)) were acquired at different positions from the CGO contact layer into 10  $\mu\text{m}$  of the electrode. Fig. 5(II) displays the position of the scans and the corresponding labels for a group of scans within a specific area of measurements defined by the arrows. One isolated spectrum A1 has been measured at the very interface with the electrolyte. Inside the Ni particle, the analysis of the spectra B4, E3, D5, G4 and H3 indicates the position of the K-edge at 8333 eV, which is the signature of metallic Ni. In the outer regions of Ni particles, the analysis of the edge position indicates a shift to 8345 eV, as for example in spectra E1, F1, E2, and E3, which implies a shift of the chemical state from Ni to  $\text{Ni}^{2+}$  and the presence of NiO. Further, in the region at the interface and close to the pores, as in spectra B2, C3, D3, D2, D1, I2 and I3, the K-edge is at 8333 eV indicating a metallic state. Within the volume analyzed, the cross-section of Ni particles is probed and the chemical state of Ni varies according to the position probed from metallic nickel (inside the grain volume) to a mixture of Ni and NiO (region of Ni in contact with CGO) and to NiO/ $\text{Ni}(\text{OH})_2$  (region in contact with CGO and pores, spectrum C3).

## 3.2. Emphasis on the degradation mechanism at the hydrogen electrode

The fuel electrode is generally the conventional cermet made of a nickel catalyst and the ceramic electrolyte material that consists of oxides with high oxide ion conductivity. To achieve a higher reaction rate, the microstructure of the fuel electrode is adjusted carefully in terms of porosity, thermal, chemical, and mechanical stability. By that, electron-conducting Ni particles are in contact with oxide ion-conducting particles or mixed-ionic-electronic conducting (MIEC) particles and open pores through which steam and hydrogen enter and leave the electrode structure. The total conductivity  $\sigma$  of the different species involved are as follows:  $\sigma = 0.054\ \text{S/cm}$  for 8YSZ,  $\sigma = 0.050\ \text{S/cm}$  for 6Sc0.5CeSZ, and  $\sigma = 0.15\ \text{S/cm}$  for CGO at 800  $^\circ\text{C}$  [33,34]. The electrochemical reaction occurs near these three phases (Ni, YSZ/CGO, and fuel gas), called the triple-phase boundary or within the entire electrode when using a MIEC. The degradation rate of CSC and ESC operated for long-term in electrolysis mode and studied in this paper can be summarized as follows.

- 10 mV/kh for a Jülich CSC, with Ni(YSZ)/8YSZ (8  $\mu\text{m}$ )/CGO/LSCF architecture operated at  $0.75\ \text{A/cm}^2$  for 6100 h at 780  $^\circ\text{C}$ , with absolute humidity AH = 80% and steam conversion SC = 40% [24].
- 7.4 mV/kh for a Kerafol ESC (commercially available but not optimized for electrolysis operation), with Ni(CGO)/CGO/6Sc1CeSZ (130  $\mu\text{m}$ )/CGO/LSCF architecture operated at  $0.9\ \text{A/cm}^2$  for 20100 h at 850  $^\circ\text{C}$ , AH = 75% and SC = 51% (total operation time is 23000 h) [25].

The state-of-the-art ESC operation with a thin electrolyte (40  $\mu\text{m}$  thick), proposed by Sunfire (who continuously optimizes the cell for electrolysis operation) has a degradation rate of 5 mV/kh for the Ni (CGO)/CGO/3 YSZ (40  $\mu\text{m}$ )/CGO/LSCF cell architecture operated at  $0.9\ \text{A/cm}^2$  for 24000 h at 852–858  $^\circ\text{C}$ , AH = 75% and SC = 60% (total operation time is 30000 h) [14].

The main source of degradation of the Ni-YSZ fuel electrode is attributed so far to the microstructural changes in the Ni network due to Ni migration as well as to the electrode overpotential. A revised hypothesis on the migration of Ni in the CSC has been proposed via surface diffusion of  $\text{Ni}(\text{OH})_x$  species below ca. 800  $^\circ\text{C}$  and via the gas phase of Ni (OH) $_x$  species above ca. 900  $^\circ\text{C}$  by Mogensen et al. [4]. The surface oxidation of nickel in NiO/CGO//8 YSZ (150  $\mu\text{m}$ )/Pt and NiO/YSZ//8 YSZ (150  $\mu\text{m}$ )/Pt model electrodes from Kerafol was studied under a constant current of  $100\ \text{mA/cm}^2$  at 640  $^\circ\text{C}$  (the temperature at which the oxidation process is not limited by the oxygen diffusion) by Mefawy et al. [11,19]. Using AP-XPS and NEXAFS, it has been shown that the surface oxidation state of nickel affects the electrical and ionic conduction as well as the reaction kinetics in Ni/YSZ, while for Ni/CGO only the electronic conduction is reduced with the formation of NiO. This implies that a few nm thick layer of NiO over metallic Ni particle will block the electrochemical cell performance in Ni/YSZ while in Ni/CGO the electrochemical reaction continues although electric losses are not negligible. Similar studies with a complete cell NiO/YSZ//8 YSZ (150  $\mu\text{m}$ )/LSCrF cell indicate that the Ni2p spectra evolves with the gas environment [35]. In  $\text{H}_2$  or  $\text{H}_2\text{O}/\text{H}_2$  mixture the Ni is metallic with the main  $\text{Ni}2p_{3/2}$  peak at 852.7 eV while Ni is oxidized to  $\text{Ni}^{2+}$  in pure  $\text{H}_2\text{O}$  atmosphere (shift of the main peak at 855.5 eV with an intense satellite at 862 eV). Although it is hard to distinguish from the Ni2p spectra between the oxide and the hydroxyl species  $\text{Ni}(\text{OH})_2$  (with  $\text{Ni}^{2+}$  oxidation state) or NiOOH (oxyhydroxide species with  $\text{Ni}^{3+}$  oxidation state) the O1s spectra clearly show that the presence of steam involves the fast decomposition of adsorbed  $\text{H}_2\text{O}$  on nickel to form NiO and not  $\text{Ni}(\text{OH})_2$  [35]. A recent comparative study of the O1s spectra on model porous Ni/CGO//YSZ//Pt electrodes and Au/CGO//YSZ//Pt tested between 570  $^\circ\text{C}$  and 650  $^\circ\text{C}$  suggests that oxide vacancy site concentrations and cation site concentrations of reduced ceria polarons are affected by the oxygen partial pressure and the surface potential. It has been shown that Ni electrodes provide higher  $\text{H}_2$  oxidation current compared to Au

electrodes. However, the Ni activity is reduced because of the increased electronic conductivity of the CGO due to the chemical state change of ceria [36].

Thus, questions remain on the nature of the intermediate species of nickel on porous electrodes operated under practical conditions. Nano-XANES has the potential to probe specifically the chemical state of nickel within the sample volume. In addition, this technique complements well the X-ray photoelectron spectroscopy that probes the surface. To the best of our knowledge, only one study using a microbeam ( $2 \times 2 \mu\text{m}^2$ ) [37] has been performed to probe the chemical state of Ni in a fractured cross-section of a tubular cell prepared for fuel cell operation to understand the interaction between the sintering temperature, the operating conditions and the nickel oxidation state. Two tubular cells, with the NiO/YSZ//10Sc1CeSZ (6  $\mu\text{m}$ )/CGO/LSCF/CGO structure, were prepared and sintered at 1300 °C and 1350 °C. The fuel cell operation was performed under diluted hydrogen (20% H<sub>2</sub> in Ar) and air for 8 h. Ni K-edge XANES spectra taken at different positions within a line from the electrolyte up to 106  $\mu\text{m}$  within the fuel electrode indicate that the chemical state of Ni was in an oxide state up to the electrolyte for the cell sintered at 1300 °C and only up to 36  $\mu\text{m}$  for the one sintered at 1350 °C.

Thus, this study provides unique results on the porous Ni/YSZ and Ni/CGO fuel electrode using a nanobeam ( $50 \times 50 \text{ nm}^2$ , allowing high-resolution compositional analysis and intra-granular changes to be probed) on samples operated for long-term (>5000 h) in electrolysis mode. The topography of the porous Ni/YSZ and Ni/CGO fuel electrodes operated under practical conditions is clearly distinct thanks to the Ni particles, the YSZ or CGO network and the pores. Ni particle sizes are in the range from 0.4 to 2.5  $\mu\text{m}$  close to the electrolyte interface and around 4–5  $\mu\text{m}$  in the substrate of the CSC operated for 6100 h. As for the ESC, larger Ni particles are present in the active layer in the size range from 0.3 to around 6  $\mu\text{m}$  after 23000 h of operation. In the as-prepared CSC, the fuel electrode is made of a dense structure of NiO and YSZ phase without any pores. The YSZ network based on the Y map does not significantly change after the 6100 h of operation, while the Ni map shows an irregular depletion of this element within 4  $\mu\text{m}$  from the electrolyte and a coarsening of the Ni particles in the substrate layer (Fig. 4(III)). For the as prepared ESC, NiO and CGO phase as well as large pores is observed with a rather dense structure of the CGO within the contact layer (Fig. 5(III)). Furthermore, a significant accumulation of Ce and Gd is observed over a few  $\mu\text{m}$  at the interface of the contact layer and electrolyte. After the operation of 23,000 h at a current density of 0.9 A/cm<sup>2</sup> and 856 °C, it can be seen that Ni is depleted from 1  $\mu\text{m}$  from the electrode/contact layer interface with a coarsening of the Ni particles. The depletion length is smaller compared to the CSC, most probably because of the diffusion of Ce and Gd in the same direction from the contact layer to the fuel electrode that blocks at an early stage the depletion of Ni by the coating of Ni particles with CGO. These results are in line with recent *operando* studies on patterned Ni-YSZ and Ni-CGO model electrodes operated in SOFC, SOEC and reversible solid oxide cell (RSOC) modes suggesting that in electrolysis mode (operation time of 60 h in potentiostatic mode of 1.5 V under 4/4/92H<sub>2</sub>/H<sub>2</sub>O/N<sub>2</sub> vol%, confocal laser scanning microscopy, resolution of 256 nm), no dynamic migration of Ni occurs in Ni-YSZ but rather coarsening and the higher contact angle detaches Ni from the YSZ surface. In contrast, for the Ni-CGO fuel electrode, it has been observed that the movement of CGO and changes in the CGO surface prevent the movement of Ni [38,39]. The higher performance of Ni/CGO has been attributed as well to the low agglomeration rate of ceria particles, which are responsible for the electrochemical reaction, while Ni fulfils the function of an electronic conductor and catalyst. The Ni depletion is independent of the electrolyte as shown by Liu et al. as a symmetrical cell based on a 200  $\mu\text{m}$  thick 8 YSZ electrolyte, CGO interlayers and Ni/CGO fuel electrodes indicate a similar behavior of Ni particles coating by cerium and gadolinium and a suppression of Ni migration [40]. Indeed, the EDX mapping acquired on the symmetrical cell aged for 240 h indicates an agglomeration of the Ni

particles together with a spreading of cerium towards the Ni/CGO electrode on the operated cell compared to the reference one. From the nano-XANES data, the chemical state of the core of the Ni particles analyzed in the volume is metallic (examples spectra: A1, E1, E2, B1, and B2) while only the outer region of the Ni particles exhibits in specific areas presence of oxidized species. In order to evaluate the ratio between the Ni, NiO and/or Ni(OH)<sub>2</sub>, a linear combination fitting using Athena's analysis tools was performed on normalized  $\mu(\text{E})$  spectra. The fit results with the R-factor are (42% Ni and 58% NiO; R = 0.014), (62% Ni and 38% NiO; R = 0.003), (76% Ni, and 24% NiO; R = 0.002), (24% Ni, 18% NiO and 58% Ni(OH)<sub>2</sub>; R = 0.01) at the position D3, D4, I3 and C3, respectively. The presence of NiO and Ni(OH)<sub>2</sub> within the fuel electrode seems to be a function of the pores and CGO particle distribution around the Ni particles and by that, it is rather inhomogeneous within the outer region of a particle. These data, taken in the volume of the sample complement the ones performed at the surface using XPS and model electrodes [11,35]. Indeed, it is suggested that mass transport path and/or mass transport species are different between Ni-YSZ and Ni-CGO as the Ni surface state is similar for both materials while the state of adsorbed oxygen differs with (OH)<sub>ad</sub> (at about 532 eV) only on the Ni surface of Ni-YSZ electrode and larger concentration of (O)<sub>ad</sub> (at about 529 eV) compared to (OH)<sub>ad</sub> in the Ni-CGO electrode [41].

This experimental work highlights the different degradation processes occurring in Ni/YSZ and Ni/CGO fuel electrodes. In the case of Ni/YSZ, Ni migration is detrimental while in the case of Ni/CGO, the diffusion of Gd and Ce from the CGO contact layer blocks the Ni depletion. This study indicates that in the case of Ni/CGO the mechanism of oxygen spillover with NiO/Ni(OH)<sub>2</sub> at the surface is more likely in contrast to Ni/YSZ. The presence of NiO is not detrimental to the electrochemical reaction of the Ni/CGO fuel electrode as shown by the 23000 h of electrochemical testing, by XPS and by in-situ impedance spectroscopy where non-ohmic losses are not as significant compared to Ni/YSZ. Further, the Ni migration seems to not involve oxide species in the case of Ni/YSZ but rather the deterioration of the contact angles between Ni and YSZ as suggested by Monaco et al. [13]. These differences in degradation mechanisms between the Ni/YSZ and Ni/CGO fuel electrodes correlate with the in-situ impedance data where the degradation is featured by the increase of the ohmic losses in both cases and of a non-ohmic loss term for the Ni/YSZ fuel electrode only. Thanks to the Ni K-edge nano-XANES acquired in combination with nano-XRF, it has been possible to spatially resolve regions specific to depletion, coarsening as well as the change in the chemical state of Ni. However, to better quantify intermediate species like Ni(OH)<sub>x</sub> at least in post-mortem samples it will be necessary in future work to stop the cell under specific conditions or to accelerate the reaction in order to increase the concentration of those species.

#### 4. Conclusions

In this study, using a combination of X-ray fluorescence and X-ray absorption spectroscopy with a spatial resolution in the nm scale, two cell architectures have been used to compare the microstructure evolution of the Ni/YSZ and Ni/CGO porous fuel electrode operated for long-term under practical conditions in electrolysis mode. Large highly resolved 2D nano-XRF maps (70  $\mu\text{m} \times 60 \mu\text{m}$ ) allowed visualizing the specific regions where Ni is depleted or coarsened to large particles. It has been shown that Ni depletion is occurring within the Ni/YSZ fuel electrode in CSC while this depletion is prevented by the movement of cerium and gadolinium elements from the CGO contact layer to the fuel electrode in ESC. Using Ni K-edge nano-XANES, it has been shown that Ni is in the metallic state in the Ni/YSZ active layer and in the substrate, while oxidized states of Ni is found on specific regions of the Ni/CGO fuel electrode. Indeed, the chemical state of Ni is metallic inside the grain volume while a mixture of Ni and NiO is found in the region of Ni in contact with CGO and Ni and NiO/Ni(OH)<sub>2</sub> in the region in contact with CGO and pores. The imaging and spectroscopy data complement

the ones from impedance spectroscopy where Ni/YSZ degradation is related to the increase of not only the ohmic losses but also the non-ohmic ones that correspond to the deactivation of the fuel electrode. In contrast, for the Ni/CGO electrode the degradation source was mainly the increase of the ohmic losses.

Within the scale up to the gigawatt range of the high temperature electrolyzers based on solid oxide cell, the electrochemical performance is continuously optimized in order to achieve stable operation at higher current density and/or reduced temperature. This experimental work highlights differences in the chemical state of Ni in Ni/YSZ and Ni/CGO suggesting specific degradation processes. The presence of the contact layer based on CGO increases the lifetime of the cell independently of the electrolyte type by a coating of the Ni particles with the diffusion of cerium and gadolinium that prevents the subsequent Ni migration. These observations suggest potential paths for a stable microstructure for electrolysis operation together with quantitative experimental data for validating the mass transport path and/or mass transport species in existing models.

### CRedit authorship contribution statement

**Aline Léon:** Investigation, Formal analysis, Supervision, and, Validation, Visualization, Funding acquisition, Writing – original draft, Writing – review & editing. **Sabine Schlabach:** Investigation, Writing – review & editing. **Julie Villanova:** Investigation, Formal analysis, Supervision, and, Validation, Visualization, Writing – review & editing.

### Declaration of competing interest

The authors declare that they have no known competing financial interests or personal relationships that could have appeared to influence the work reported in this paper.

### Data availability

Data will be made available on request.

### Acknowledgements

The authors kindly acknowledge KNMFi for the acceptance of our proposal 2016-017-016089 related to the FIB sample preparation. We thank ESRF for beamtime given under MA-3257 proposals and in-house resources. The authors acknowledge the support from the project H2GiGa, DegradEL<sup>3</sup> (Grant: 03HY110C) funded by the German Federal Ministry of Education and Research. The authors acknowledge sincerely J. Schefold for the discussions and for providing the long-term tested cells in the frame of German projects Horizont (Grant: 03 ET2014C) and Sunfire (Grant: 01RC1110) funded by the German Federal Ministry of Economics & Technology and the German Federal Ministry of Education & Research, respectively. The authors express their sincere thanks to F. Tietz (FZJ) and H. Poepke (Kerafol) for providing the reference samples.

### References

- [1] E. Iea, IEA, Paris, 2022. <https://www.iea.org/reports/electrolysers>. License: CC BY 4.0.
- [2] S.J. McPhail, S. Frangini, J. Laurencin, E. Effori, A. Abaza, A.K. Padinjarethil, et al., Addressing planar solid oxide cell degradation mechanisms: a critical review of selected components, *Electrochem. Sci. Adv.* 2 (2021).
- [3] A. Brisse, J. Schefold, A. Léon, High-temperature steam electrolysis, in: Tom Smolinka & Jürgen Garche, Chapter 7, 2021, pp. 229–280.
- [4] M.B. Mogensen, M. Chen, H.L. Frandsen, C. Graves, A. Hauch, P.V. Hendriksen, et al., Ni migration in solid oxide cell electrodes: review and revised hypothesis, *Fuel Cells* 21 (2021) 415–429.
- [5] M.S. Sohal, J.E. O'Brien, C.M. Stoots, V.I. Sharma, B. Yildiz, A. Virkar, Degradation issues in solid oxide cells during high temperature electrolysis, *J. Fuel Cell Sci. Technol.* 9 (2012).
- [6] A. Hauch, R. Kungas, P. Blennow, A.B. Hansen, J.B. Hansen, B.V. Mathiesen, et al., Recent advances in solid oxide cell technology for electrolysis, *Science* 370 (Oct 9 2020).
- [7] D. Wiedenmann, A. Hauch, B. Grobety, M. Mogensen, U.F. Vogt, Complementary techniques for solid oxide electrolysis cell characterisation at the micro- and nano-scale, *Int. J. Hydrogen Energy* 35 (2010) 5053–5060.
- [8] A. Stangl, D. Muñoz-Rojas, M. Burriel, In situ and operando characterisation techniques for solid oxide electrochemical cells: recent advances, *J. Phys.: Energy* 3 (2020), 012001.
- [9] M. Riegraf, R. Costa, G. Schiller, K.A. Friedrich, S. Dierickx, A. Weber, Electrochemical impedance analysis of symmetrical Ni/Gadolinium-Doped ceria (CGO10) electrodes in electrolyte-supported solid oxide cells, *J. Electrochem. Soc.* 166 (2019) F865–F872.
- [10] M. Trini, P.S. Jørgensen, A. Hauch, J.J. Bentzen, P.V. Hendriksen, M. Chen, 3D microstructural characterization of Ni/YSZ electrodes exposed to 1 Year of electrolysis testing, *J. Electrochem. Soc.* 166 (2019) F158–F167.
- [11] B. Mewafy, F. Paloukis, K.M. Papazisi, S.P. Balomenou, W. Luo, D. Teschner, et al., Influence of surface state on the electrochemical performance of nickel-based cermet electrodes during steam electrolysis, *ACS Appl. Energy Mater.* 2 (2019) 7045–7055.
- [12] D. The, S. Grieshammer, M. Schroeder, M. Martin, M. Al Daroukh, F. Tietz, et al., Microstructural comparison of solid oxide electrolyser cells operated for 6100 h and 9000 h, *J. Power Sources* 275 (Feb 1 2015) 901–911.
- [13] F. Monaco, M. Hubert, J. Vulliet, J.P. Ouweltjes, D. Montinaro, P. Cloetens, et al., Degradation of Ni-YSZ electrodes in solid oxide cells: impact of polarization and initial microstructure on the Ni evolution, *J. Electrochem. Soc.* 166 (2019) F1229–F1242.
- [14] J. Schefold, A. Léon, 30,000 hours steam electrolysis with a 3YSZ electrolyte supported cell at elevated current density, *Proc. 15th Eur. SOFC & SOEC Forum* B0604 (2022) 282.
- [15] R. Kiebach, K. Norrman, C. Chatzichristodoulou, M. Chen, X. Sun, S.D. Ebbesen, et al., TOF-SIMS characterization of impurity enrichment and redistribution in solid oxide electrolysis cells during operation, *Dalton Trans.* 43 (Oct 28 2014) 14949–14958.
- [16] M. Kusnezoff, N. Trofimenko, M. Muller, A. Michaelis, Influence of electrode design and contacting layers on performance of electrolyte supported SOFC/SOEC single cells, *Materials* 9 (Nov 8 2016).
- [17] Q. Zhang, P. Voorhees, S. Barnett, Modeling of Ni migration in Ni-YSZ electrodes during solid oxide electrolysis, in: 15th European SOFC & SOEC Forum, Vol. Proceedings of the Conference B1103, 2022, p. 454.
- [18] L. Rorato, Y. Shang, S. Yang, M. Hubert, K. Couturier, L. Zhang, et al., Understanding the Ni migration in solid oxide cell: a coupled experimental and modeling approach, *J. Electrochem. Soc.* 170 (2023), 034504.
- [19] V. Papaefthimiou, D.K. Niakolas, F. Paloukis, D. Teschner, A. Knop-Gericke, M. Haeverker, et al., Operando observation of nickel/ceria electrode surfaces during intermediate temperature steam electrolysis, *J. Catal.* 352 (2017) 305–313.
- [20] J. Villanova, S. Schlabach, A. Brisse, A. Léon, X-ray fluorescence nano-imaging of long-term operated solid oxide electrolysis cells, *J. Power Sources* 421 (2019) 100–108.
- [21] A. Nakajo, G. Rinaldi, P. Caliendo, G. Jeanmonod, L. Navratilova, M. Cantoni, et al., Evolution of the morphology near triple-phase boundaries in Ni-yttria stabilized zirconia electrodes upon cathodic polarization, *J. Electrochem. Energy Conversion Storage* 17 (2020).
- [22] S. Yang, J. Gao, M. Trini, S. De Angelis, P.S. Jørgensen, J.R. Bowen, et al., Ni coarsening in Ni-yttria stabilized zirconia electrodes: three-dimensional quantitative phase-field simulations supported by ex-situ ptychographic nanotomography, *Acta Mater.* 246 (2023), 118708.
- [23] F. El Gabaly, K.F. McCarty, H. Blumh, A.H. McDaniel, Oxidation stages of Ni electrodes in solid oxide fuel cell environments, *Phys. Chem. Chem. Phys.* 15 (Jun 7 2013) 8334–8341.
- [24] J. Schefold, A. Brisse, Steam electrolysis in reversibly operated SOFC: long-term cell testing beyond 1000 h, *ECS Trans.* 53 (2013) 53.
- [25] J. Schefold, A. Brisse, H. Poepke, 23,000 h steam electrolysis with an electrolyte supported solid oxide cell, *Int. J. Hydrogen Energy* 42 (2017) 13415–13426.
- [26] G. Martinez-Criado, J. Villanova, R. Tucoulou, D. Salomon, J.P. Suuronen, S. Laboure, et al., ID16B: a hard X-ray nanoprobe beamline at the ESRF for nano-analysis, *J. Synchrotron Radiat.* 23 (Jan 2016) 344–352.
- [27] R.M. Trevorah, C.T. Chantler, M.J. Schalken, Solving self-absorption in fluorescence, *IUCrJ* 6 (Jul 1 2019) 586–602.
- [28] B. Ravel, M. Newville, ATHENA, artemis, hephaestus: data analysis for X-ray absorption spectroscopy using IFEFFIT, *J. Synchrotron Radiat.* 12 (Jul 2005) 537–541.
- [29] A.M. Beale, M. Paul, G. Sankar, R.J. Oldman, C.R.A. Catlow, S. French, et al., Combined experimental and computational modelling studies of the solubility of nickel in strontium titanate, *J. Mater. Chem.* 19 (2009) 4391.
- [30] K. Tirez, G. Silversmit, L. Vincze, K. Servaes, C. Vanhoof, M. Mertens, et al., Speciation and fractionation of nickel in airborne particulate matter: comparison between selective leaching and XAS spectroscopy, *J. Anal. At. Spectrom.* 26 (2011) 517–527.

- [31] J. Vaughan, J. Riggio, J. Chen, H. Peng, H.H. Harris, A. van der Ent, Characterisation and hydrometallurgical processing of nickel from tropical agromined bio-ore, *Hydrometallurgy* 169 (2017) 346–355.
- [32] J.K. Kesavan, I. Luisetto, S. Tuti, C. Meneghini, C. Battocchio, G. Iucci, Ni supported on YSZ: XAS and XPS characterization and catalytic activity for CO<sub>2</sub> methanation, *J. Mater. Sci.* 52 (2017) 10331–10340.
- [33] J.W. Fergus, Electrolytes for solid oxide fuel cells, *J. Power Sources* 162 (2006) 30–40.
- [34] M. Kusnezoff, M. Jahn, S. Megel, S. Rothe, S. Hielscher, E. Reichelt, et al., Progress in SOC development at fraunhofer IKTS, *ECS Trans.* 103 (2021) 307.
- [35] F. Paloukis, K.M. Papazisi, T. Dintzer, V. Papaefthimiou, V.A. Saveleva, S. P. Balomenou, et al., Insights into the surface reactivity of cermet and perovskite electrodes in oxidizing, reducing, and humid environments, *ACS Appl. Mater. Interfaces* 9 (Aug 2 2017) 25265–25277.
- [36] L. Wang, Y. Yu, K.J. Gaskell, E.J. Crumlin, Z. Liu, B.W. Eichhorn, et al., "In operando x-ray photoelectron spectroscopy studies of H<sub>2</sub> oxidation and H<sub>2</sub>O electrolysis on gadolinia-doped ceria electrodes," *J. Phys.: Energy* 3 (2020), 014004.
- [37] K. Hamamoto, T. Suzuki, B. Liang, T. Yamaguchi, H. Sumi, Y. Fujishiro, et al., INVESTIGATION OF NI-YTTRIA STABILIZED ZIRCONIA ANODE FOR SOLID-OXIDE FUEL CELL USING XAS ANALYSIS, in: Prabhakar Singh, P. Narottam, Bansal (Eds.), *Advances in Solid Oxide Fuel Cells VIII*, vol. 137, 2012.
- [38] Y. Komatsu, A. Sciazko, Y. Suzuki, Z. Ouyang, Z. Jiao, N. Shikazono, Operando observation of patterned nickel-gadolinium doped ceria solid oxide fuel cell anode, *J. Power Sources* 516 (2021).
- [39] Z. Ouyang, Y. Komatsu, A. Sciazko, J. Onishi, K. Nishimura, N. Shikazono, Operando observations of active three phase boundary of patterned nickel-yttria stabilized zirconia electrode in solid oxide cell, *J. Power Sources* 529 (2022).
- [40] Y. Liu, F. Wankmüller, M. Juckel, A. Weber, Accelerated testing of microstructural degradation in nickel-ceria fuel electrodes structure, in: *Proceedings of the Conference of the 15th European SOFC & SOEC Forum B0602*, 2022.
- [41] H. Kishimoto, T. Shimonosono, K. Yamaji, M. Brito, T. Horita, H. Yokokawa, Oxide component in the nickel base cermet anode: its effect on the performance of SOFCs, *Electrochemistry* 81 (2013).